Proceedings of CONF-MLA 2026 Symposium: Intelligent Systems and Automation: AI Models, IoT, and Robotic Algorithms
DOI: 10.54254/2755-2721/2026.LD39393

A Co-design Method for Taper and Actuation Distribution in Bioinspired Soft Robotic Arms

Zesheng Zhang

Canada British Columbia International Schools-Chengdu, Beihu Campus, Chengdu, China
z2220783496@outlook.com

Abstract. Biological continuum appendages taper along their length, yet soft robotic arms are commonly uniform cylinders, and existing design optimization fixes the morphology before the actuation. This paper proposes a co-design method that places taper ratio, taper concentration and actuation decay index in one three-parameter analytical design space at fixed material volume. Each design is evaluated by a quasi-static Cosserat rod model that imposes the target pose as a boundary condition and treats the actuation amplitude as an unknown, so one solution returns both objectives: actuation work and tip displacement under payload. Over seven payload-to-self-weight ratios from 0.10 to 1.60, a tapered morphology dominates the uniform arm on both objectives, NSGA-II joint search attains a larger Pareto hypervolume than equal-budget sequential search, and the knee-point taper ratio falls as the payload ratio rises, giving a closed-form rule for selecting the taper.

Keywords: soft robotics, bioinspired design, Cosserat rod, taper ratio, multi-objective design optimization

1. Introduction

Biological arms taper. Sun et al. [1] show that the octopus arm is a muscular hydrostat whose cross-sectional area decreases from base to tip. Kodama et al. [2] note that most soft robotic arms move compliantly but lack load capacity, and propose an elephant-trunk-inspired arm that combines pneumatic force bags with hydraulic artificial muscles.

Self-weight and payload limit the practical use of a soft robotic arm. Yang et al. [3] stiffen the arm on demand with supercoiled polymer muscles and shape memory alloys, and Zhang and Wu [4] combine compliance and high load capacity in one trunk-like structure. Li et al. [5] report a tapered manipulator with precision and load capacity, but its taper is copied from a biological outline, leaving open how a given volume should be placed along the arm.

Design optimization for soft robots fixes morphology and actuation in separate steps: Chi and Liu [6] synthesize actuator chambers by topology optimization, Tsompanas and Balaz [7] search modular morphologies with an evolutionary generator, and Moutousi and Polygerinos [8] tune actuators on a fixed morphology. Chen et al. [9] and Tan et al. [10] optimize morphology, control or gait for locomotion, without self-weight or tip payload in the objective.

This paper chooses taper and actuation distribution together, in an analytic three-parameter design space at fixed material volume and pose task, evaluated by a quasi-static Cosserat rod model

© 2026 The Authors. This is an open access article distributed under the terms of the Creative Commons Attribution License 4.0 (https://creativecommons.org/licenses/by/4.0/).

DOI: 10.54254/2755-2721/2026.LD39393

and searched by NSGA-II against an equal-budget sequential search. The contributions are the design space with its verified evaluation model, a fixed-volume comparison of tapered and uniform arms, and a design rule for the taper ratio.

2. Literature review

2.1. The taper morphology of the biological arm and its engineering

The octopus arm combines a base-to-tip decrease in cross-section with position-dependent muscle layers [1]. Engineering arms copy this taper on a single prototype, either as a fixed biomimetic profile [5] or as chamber sizes that decrease toward the tip of a segmented pneumatic arm [11], so the reported values cannot be compared from study to study.

2.2. Three routes and costs for soft arm design optimization

Soft robot design optimization follows three routes. Finite element evaluators support topology optimization of actuator chambers [6] at the cost of one finite element solution per evaluation; reduced-order models such as that of Sayadi et al. [12] make a large design space searchable; and modular discrete spaces searched by an evolutionary generator [7] leave a continuous taper ratio outside the search. In all three the objective is workspace and bending [8] or gait manoeuvrability [9], and self-weight and payload enter neither.

2.3. Cosserat rod model as an evaluator in the design stage

The Cosserat rod describes a continuum robot by position and cross-sectional pose along the arc length in a geometrically exact way. Xun et al. [13] built a Cosserat model of soft slender robots with frictional contact, Gazzola et al. [14] solved forward and inverse problems of soft filaments, and Alkayas et al. [15] reduced strain-based models for online use, whereas constant curvature needs correction once curvature varies under self-weight [12]. Since self-weight, payload and actuation enter the equilibrium equation as separate load terms, one quasi-static solution returns the state of the whole arm, which suits the design stage.

2.4. Hypotheses

The gaps above yield three propositions. H1: at fixed material volume, a taper ratio below unity lowers actuation work and tip displacement under payload relative to a uniform arm. H2: joint optimization of the three parameters attains a larger Pareto hypervolume than sequential optimization under an equal evaluation budget. H3: for a fixed pose task, the knee-point taper ratio decreases monotonically as the payload-to-self-weight ratio grows.

DOI: 10.54254/2755-2721/2026.LD39393

3. Methodology

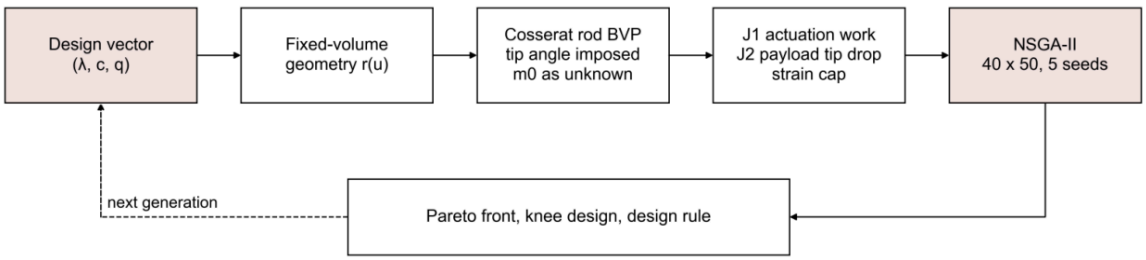

Figure 1. Flow of the proposed co-design method

3.1. Quasi-static Cosserat rod model and positional inverse solution

Figure 1 summarizes the method. The arm is treated as a planar quasi-static Cosserat rod, so that self-weight, tip load and distributed actuation moment density enter one equilibrium system. With arc length s from 0 to L, position (x, y), cross-section rotation θ, internal force (n_x, n_y), internal moment M and primes denoting derivatives in s, the governing equations are

$$x' = \nu_1 cos\theta - \nu_2 sin\theta,\ y' = \nu_1 sin\theta + \nu_2 cos\theta,\ \theta' = \frac{M}{EI(s)}, \tag{1}$$

$$n_x' = 0,\ n_y' = \rho g A(s),\ M' = -(x' n_y - y' n_x) - m(s),$$

where $\nu_1 = 1 + N/(EA(s))$ and $\nu_2 = Q/(GA_s(s))$ are the extension and shear strain measures, $N = n_x cos\theta + n_y sin\theta$ and $Q = -n_x sin\theta + n_y cos\theta$ are the axial and shear components of the internal force, E is the elastic modulus, G is the shear modulus, $A(s)$ and $I(s)$ are the cross-sectional area and the second moment of area, $A_s(s)$ is the shear-effective area, ρ is the density, g is the gravitational acceleration, and $m(s)$ is the distributed actuation moment density. The base is clamped, $x(0) = y(0) = \theta(0) = 0$. The tip is free and carries a vertical downward load W_p, which gives $n_x(L) = 0$, $n_y(L) = -W_p$ and $M(L) = 0$.

The target pose is imposed as a boundary condition: a seventh condition, $\theta(L) = \theta_t$, prescribes the tip rotation, and the actuation amplitude m_0 scaling $m(s)$ is an unknown parameter, so one solution delivers the actuation amplitude together with the shape and internal loads. The problem is solved with SciPy solve_bvp on meshes of 241, 481 and 961 nodes (tolerance 1e-6).

3.2. Three-parameter design space of taper and drive distribution

The three design variables are taper ratio λ, taper concentration c and actuation decay index q. The radius distribution along the normalized arc length $u = s/L$ and the actuation couple density are given by

$$r(u) = r_0[\lambda + (1-\lambda)(1-u)e^{-cu}], \qquad m(u) = m_0 e^{-qu} \tag{2}$$

where r_0 is the base radius, λ is the tip-to-base radius ratio ($\lambda = 1$: uniform cross-section), c sets how strongly the taper concentrates toward the base ($c = 0$: linear cone), and q is the decay rate of actuation density from base to tip ($q = 0$: uniform actuation).

DOI: 10.54254/2755-2721/2026.LD39393

All designs share the same material volume $V = \int_0^L \pi r^2 ds$, which inversely fixes the base radius:

$$r_0 = \sqrt{\frac{V}{\pi L I_2}}, \qquad I_2 = \int_0^1 [\lambda + (1-\lambda)(1-u)e^{-cu}]^2 du \tag{3}$$

Here, I_2 is calculated using 240-point Gauss–Legendre quadrature.

3.3. Dual goals, constraints and two dimensionless frameworks

The first objective is the actuation work $J_1 = \int_0^L |m(s)\kappa(s)| ds$ needed to reach the target pose $\theta_t = 90^\circ$ without load, where $\kappa = M/(EI)$ is the curvature. The second objective J_2 is the tip displacement caused by the payload W_p at that pose, normalized by arm length. Manufacturability limits the outer-fibre bending strain, $\max_s |\kappa(s)| r(s) \le 0.35$. The full problem is

$$\min_{(\lambda,c,q)\in\Theta} \{J_1,\ J_2\} \quad \text{s.t. } \max_s |\kappa(s)| r(s) \le \varepsilon_{max},\ V = \text{const} \tag{4}$$

where $\varepsilon_{max} = 0.35$ is the strain limit, and the design space Θ takes λ from 0.25 to 1 and c and q from 0 to 4.

The elasto-gravitational number $\Gamma = 4\rho g L^3/(E r_0^2)$ measures bending stiffness against self-weight, and the payload ratio $\Pi = W_p/(\rho g V)$ measures tip load relative to self-weight. The benchmark takes $L = 0.20$ m, $r_0 = 15$ mm, $E = 1.0$ MPa, $\rho = 1070$ kg/m³ and $\nu = 0.5$, giving $\Gamma = 1.49$ and a self-weight of 1.48 N; Π takes seven levels between 0.10 and 1.60.

3.4. Search scheme, comparison and model verification

The joint search uses NSGA-II[16] (pymoo 0.6.2 implementation[17]) with a population of 40, 50 generations, five random seeds per load level and 2,000 evaluations per run. The sequential search spends the same budget in two stages of 40 × 25: it searches the morphology (λ, c) under uniform actuation ($q = 0$) and keeps its Pareto knee morphology, then searches only q. The uniform arm $(\lambda, c, q) = (1, 0, 0)$ is the baseline. Front quality is measured by hypervolume with a shared reference point per load level; the knee point is the normalized-front point farthest from the line joining the front endpoints.

The model is verified in three ways: Eq. (1) reduced to zero gravity with a tip force is compared with the elliptic-integral solution[18] of the large-deflection cantilever; a uniform rod under a uniform couple is compared with the closed form $\theta(L) = m_0 L^2/(2EI)$; and the same tapered arm is relaxed to static equilibrium in the open-source Cosserat rod solver PyElastica[19], with the tip position compared at 40, 80 and 160 elements.

4. Results

4.1. Model verification

All three checks fall within tolerance. Against the elliptic-integral solution ($\alpha = PL^2/EI$ from 0.5 to 4.0) the maximum tip deviation is $1.85 \times 10^{-4} L$; against the uniform-couple closed form the maximum relative error is 1.1×10^{-16}. PyElastica shows first-order convergence: the tip deviation at 40, 80 and 160 elements is 0.89%, 0.45% and 0.23% of arm length for the uniform arm and

DOI: 10.54254/2755-2721/2026.LD39393

0.17%, 0.09% and 0.05% for the tapered arm ($\lambda = 0.35$). On the finest grid (961 nodes, tolerance 10^{-9}) the objectives of the seven knee designs change by at most 9.3×10^{-9} and 3.0×10^{-6}. One evaluation takes 9.4 ms on average over 400 random designs.

4.2. Dual target gain of the taper shape relatively uniform arm

At every one of the seven load levels a tapered design beats the uniform arm on both objectives. For the design with the largest combined improvement, actuation work is 19.7% to 48.1% lower and tip displacement under payload 2.4% to 21.4% lower (Table 1, columns 2 to 4), supporting H1. With the elasto-gravitational number doubled, all five seeds ($\Gamma = 2.99$) yield a front that dominates the uniform arm; with it halved ($\Gamma = 0.75$), four of the five do.

Table 1. Designs found by the joint search at each payload ratio, against the uniform arm of the same material volume

Payload ratio	Taper ratio	dJ1 (%)	dJ2 (%)	Knee taper	Knee dJ1 (%)	Knee dJ2 (%)	HV gain (%)
0.10	0.381	-23.0	-5.5	0.562	+1.4	-19.6	+22.8
0.15	0.353	-26.4	-2.4	0.560	+2.2	-20.7	+23.4
0.25	0.376	-24.9	-4.1	0.545	+9.1	-23.6	+25.0
0.40	0.369	-22.3	-8.2	0.501	+0.3	-24.2	+24.1
0.65	0.327	-19.7	-15.7	0.509	+2.2	-30.1	+24.6
1.00	0.251	-36.7	-11.4	0.508	+7.3	-40.2	+40.2
1.60	0.250	-48.1	-21.4	0.251	-36.5	-30.5	+39.8

Note. dJ1 and dJ2 are changes in the two objectives relative to that arm; columns 2 to 4 give the front member with the largest combined improvement, columns 5 to 7 the knee design of the same front, and the last column the hypervolume gain of joint over sequential search.

4.3. Joint optimization of the gain of relative step-by-step optimization

The joint search attains a higher hypervolume than the equal-budget sequential search in all 35 runs (7 load levels × 5 seeds), by 33.0% on average (Wilcoxon signed-rank test, $p=2.9\times10^{-11}$), so H2 holds. The gain ranges from 22.8% to 40.2% and is largest when the payload equals the self-weight ($\Pi = 1.00$; Figure 2(b)). At $\Pi = 0.40$ (Figure 2(a)) the joint front has 147 non-dominated points and the sequential front 60, of which 54 are dominated by the joint front.

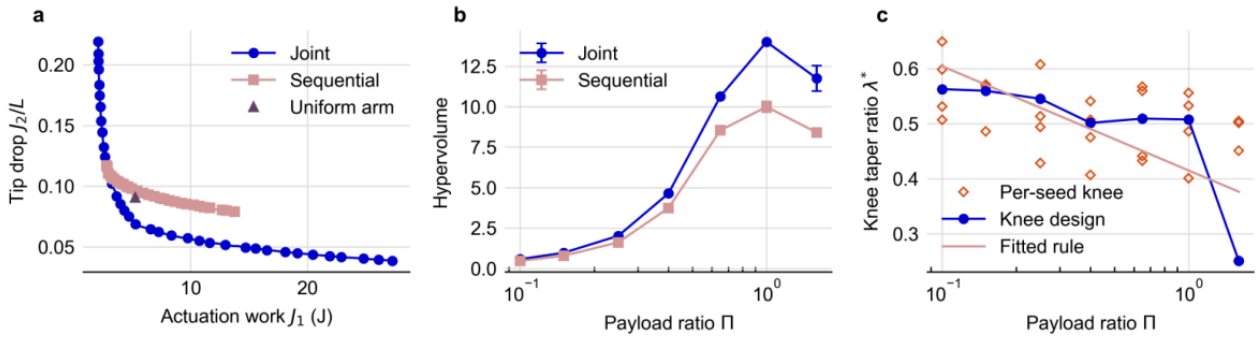

Figure 2. Pareto fronts at a payload ratio of 0.40 (a), hypervolume of joint and sequential search across payload ratios, mean and standard deviation over five seeds (b), and the knee taper ratio against the payload ratio with the fitted design rule (c)

DOI: 10.54254/2755-2721/2026.LD39393

4.4. The optimal taper ratio changes with the load-weight ratio

The knee-point taper ratio decreases from 0.562 to 0.251 as Π increases from 0.10 to 1.60 (Spearman correlation −0.893, p=0.0068), so H3 holds. A log-linear fit gives the design rule:

$$\lambda^* = 0.415 - 0.082 \ln \Pi \tag{5}$$

where λ^* is the knee-point taper ratio and Π the payload-to-self-weight ratio ($R^2 = 0.578$, p=0.047). The fit is loose because the change is concentrated at the highest load level (Figure 2(c)); the seed-to-seed standard deviation of the knee-point taper ratio is 0.037 to 0.109, largest at $\Pi = 1.60$.

5. Discussion

The taper ratio decreases with payload because of the bending-moment distribution: at fixed volume, moving material from tip to base adds second moment of area where the bending moment is largest, and a heavier payload steepens the moment gradient. The robustness test agrees: with Γ halved, the knee-point taper ratio of the five seeds rises to 0.540 to 0.611, and with Γ doubled it falls to 0.363 to 0.525.

The actuation decay index is almost inactive: its knee-point value does not exceed 0.14 at any load level, so the gain of joint over sequential optimization comes from the wider Pareto front opened by morphological variation, not from the actuation distribution itself.

6. Conclusion

At fixed material volume and pose task, a tapered morphology lowers actuation work and tip displacement under payload relative to the uniform arm at all seven payload ratios, by up to 48.1% and 21.4%; H1 holds. Joint optimization attains a Pareto hypervolume 33.0% above equal-budget sequential optimization on average; H2 holds. The knee-point taper ratio falls with the payload ratio as $\lambda^* = 0.415 - 0.082 \ln \Pi$; H3 holds.

These conclusions hold for planar quasi-static soft arms of fixed volume with bending strain below 0.35 (H1 checked at elasto-gravitational numbers 0.75, 1.49 and 2.99, H2 and H3 at 1.49), and Eq. (5) gives an initial taper ratio for a local joint search.

Torsion, contact and inertia, an alternating morphology-actuation baseline, stiffer arms, and mapping onto a 3D-printable pneumatic actuator [20] are left for future work.

References

[1] Sun, Y., et al. (2025). Real-time dynamics of soft manipulators with cross-sectional inflation: Application to the octopus muscular hydrostat. *Proceedings of the Royal Society A, 481*(2314), Article 20240642. https://doi.org/10.1098/rspa.2024.0642

[2] Kodama, H., et al. (2026). Elephant-trunk-inspired power soft robotic arm. *IEEE Robotics and Automation Letters, 11*(8), 9479–9486. https://doi.org/10.1109/lra.2026.3701119

[3] Yang, Y., et al. (2024). A variable stiffness soft robotic manipulator based on antagonistic design of supercoiled polymer artificial muscles and shape memory alloys. *Sensors and Actuators A: Physical, 366*, Article 114999. https://doi.org/10.1016/j.sna.2023.114999

[4] Zhang, J., & Wu, J. (2024). A compliant and strong robotic manipulator that looks and works like an elephant trunk. *Device, 2*(9), Article 100522. https://doi.org/10.1016/j.device.2024.100522

[5] Li, X., et al. (2024). Biomimetic tapered soft manipulator with precision and load-bearing capacity. *Cell Reports Physical Science, 5*(10), Article 102210. https://doi.org/10.1016/j.xcrp.2024.102210

DOI: 10.54254/2755-2721/2026.LD39393

[6] Chi, J. C., & Liu, C. H. (2025). Topology optimization of a soft pneumatic actuator considering design-dependent loads. *IEEE/ASME Transactions on Mechatronics, 30*(4), 2853–2861. https://doi.org/10.1109/tmech.2025.3562663
[7] Tsompanas, M. A., & Balaz, I. (2024). Outline of an evolutionary morphology generator towards the modular design of a biohybrid catheter. *Frontiers in Robotics and AI, 11*, Article 1337722. https://doi.org/10.3389/frobt.2024.1337722
[8] Moutousi, M., & Polygerinos, P. (2024). Omnidirectional soft pneumatic actuators: A design and optimization framework. *Frontiers in Robotics and AI, 11*, Article 1418484. https://doi.org/10.3389/frobt.2024.1418484
[9] Chen, C., et al. (2024). Deep reinforcement learning based co-optimization of morphology and gait for small-scale legged robot. *IEEE/ASME Transactions on Mechatronics, 29*(4), 2697–2708. https://doi.org/10.1109/tmech.2023.3330427
[10] Tan, K., et al. (2025). Optimal gait design for a soft quadruped robot via multi-fidelity Bayesian optimization. *Applied Soft Computing, 169*, 112568. https://doi.org/10.1016/j.asoc.2024.112568
[11] Papadakis, E., Tsakiris, D. P., & Sfakiotakis, M. (2024). An octopus-inspired soft pneumatic robotic arm. *Biomimetics, 9*(12), 773. doi: 10.3390/biomimetics9120773.
[12] Sayadi, A., Cecere, R., & Hooshiar, A. (2024). Finite arc method: Fast-solution extended piecewise constant curvature model of soft robots with large variable curvature deformations. *Robot. Rep., 2*(1), 49-64. doi: 10.1089/rorep.2023.0028.
[13] Xun, L., Zheng, G., & Kruszewski, A. (2024). Cosserat-rod-based dynamic modeling of soft slender robot interacting with environment. *IEEE Trans. Robot., 40*, 2811-2830. doi: 10.1109/tro.2024.3386393.
[14] Gazzola, M., et al. (2018). Forward and inverse problems in the mechanics of soft filaments. *Roy. Soc. Open Sci., 5*(6), 171628. doi: 10.1098/rsos.171628.
[15] Alkayas, A. Y., et al. (2025). Soft synergies: Model order reduction of hybrid soft-rigid robots via optimal strain parameterization. *IEEE Trans. Robot., 41*, 1118-1137. doi: 10.1109/tro.2024.3522182.
[16] Deb, K., et al. (2002). A fast and elitist multiobjective genetic algorithm: NSGA-II. *IEEE Transactions on Evolutionary Computation, 6*(2), 182–197. https://doi.org/10.1109/4235.996017
[17] Blank, J., & Deb, K. (2020). Pymoo: Multi-objective optimization in Python. *IEEE Access, 8*, 89497–89509. https://doi.org/10.1109/access.2020.2990567
[18] Bisshopp, K. E., & Drucker, D. C. (1945). Large deflection of cantilever beams. *Quarterly of Applied Mathematics, 3*(3), 272–275. https://doi.org/10.1090/qam/13360
[19] Naughton, N., et al. (2021). Elastica: A compliant mechanics environment for soft robotic control. *IEEE Robotics and Automation Letters, 6*(2), 3389–3396. https://doi.org/10.1109/lra.2021.3063698
[20] Gunawardane, P. D. S. H., et al. (2024). A versatile 3D-printable soft pneumatic actuator design for multi-functional applications in soft robotics. *Soft Robotics, 11*(4), 709–723. https://doi.org/10.1089/soro.2023.0102